Journal of Alloys and Compounds 831 (2020) 154891

Contents lists available at ScienceDirect

Journal of Alloys and Compounds

journal homepage: http://www.elsevier.com/locate/jalcom

High-pressure torsion processing of Zn–3Mg alloy and its hybrid counterpart: A comparative study

David Hernández-Escobar [a, *], Raymond R. Unocic [b], Megumi Kawasaki [c], Carl J. Boehlert [a]

[a] Department of Chemical Engineering and Materials Science, Michigan State University, East Lansing, MI, 48824, USA
[b] Center for Nanophase Materials Sciences, Oak Ridge National Laboratory, Oak Ridge, TN, 37831, USA
[c] School of Mechanical, Industrial and Manufacturing Engineering, Oregon State University, Corvallis, OR, 97331, USA

ARTICLE INFO

Article history:
Received 15 January 2020
Received in revised form
5 March 2020
Accepted 21 March 2020
Available online 23 March 2020

Keywords:
Heterostructure
High-pressure torsion
Hybrid
Intermetallic
Microhardness
Zinc

ABSTRACT

Processing of metal hybrid nanocomposites have emerged in the recent years by means of solid-state reactions through severe plastic deformation techniques, resulting in heterogenous microstructures and mechanical properties. Despite the increased scientific interest in these unusual materials, little is known regarding their comparative attributes with respect to a homogeneous material having equivalent nominal composition. This work provides a direct comparison of the microstructure and the hardness evolution between a Zn–3Mg (wt.%) alloy and its hybrid counterpart, after high-pressure torsion (HPT) and after HPT followed by a post-deformation annealing (PDA) treatment. Experimental results indicate that both the alloy and the hybrid reach a similar level of grain refinement after HPT processing, however, grain growth follows different trends after PDA. The HPT-processed alloy exhibits clusters of Mg_2Zn_{11} nanocrystalline domains that coalesce into coarser grains maintaining a unimodal GS distribution after PDA. On the other hand, the hybrid after PDA displays a multimodal GS distribution consisting of ultrafine Mg-rich grains containing $MgZn_2$ and Mg_2Zn_{11} nanoscale intermetallics, in a matrix of coarser dislocation-free Zn grains. These observations were supported by kernel average misorientation (KAM) maps and pole figures obtained through electron backscattered diffraction (EBSD) analysis.

1. Introduction

Metal hybrid systems with heterogeneous microstructures, including Al-Cu [1–3], Al-Mg [4,5], Al-Fe [6], Al-Ti [6], Zn-Mg [7,8], Cu-Ta [9] and Cu–ZnO [10], among others, have been synthesized in recent years by means of solid-state reactions through the application of severe plastic deformation (SPD) processes. One of the most efficient SPD techniques, in terms of grain refinement, is high-pressure torsion (HPT) [11]. During conventional HPT, a disk-like shaped specimen (typically 10 mm diameter and ~1 mm thickness) is simultaneously subjected to a large hydrostatic pressure (usually 6 GPa) and severe torsional straining. The combined action of compressive and shear stresses generates a significant amount of point and line defects within the specimen, promoting fast atomic mobility even at room temperature (RT) [12]. Such defects, lead to exceptional strengthening and hardening, thereby promoting more interest in HPT. Although HPT was initially performed on pure metals [13–20], it was later used for solidified alloys [21–24] and then for the mechanical bonding of dissimilar metal disks laid on top of each other, where the output is termed a HPT hybrid [1–9]. In addition, consolidation of machining chips [25–27] and metallic powders [28–31], as well as the processing of metal oxides [32] and semiconductor materials [33] has been achieved through HPT.

Despite the different types of synthesis approaches arising from the application of the same HPT principles, a direct comparison between a HPT-processed alloy (hereinafter termed “HPT alloy”), and its HPT-processed hybrid (hereinafter termed “HPT hybrid”) counterpart is lacking. This work compares the microstructural and hardness evolution of two different HPT-processed materials, each having a nominal composition of Zn–3Mg (wt %), both after HPT and after HPT followed by a post-deformation annealing (PDA) treatment. This comparison is intended to determine whether HPT-processed hybrid structures offer advantages over HPT-processed alloys in terms of grain refinement and hardening mechanisms.

* Corresponding author. 428 S Shaw Lane, 2100, East Lansing, MI, 48824, USA.
E-mail address: herna437@egr.msu.edu (D. Hernández-Escobar).

https://doi.org/10.1016/j.jallcom.2020.154891
0925-8388/

2. Experimental material and methods

2.1. Sample preparation

HPT was performed using the following three materials: Zn−3Mg (wt.%) casting, commercially pure Zn (99.97% purity, Goodfellow Inc, Coraopolis, PA), and commercially pure Mg (99.90% purity, Goodfellow Inc, Coraopolis, PA). All compositions are provided in wt.% unless otherwise stated. The materials were received in the form of 10 mm diameter cast bars, from which a series of disks samples with specific thicknesses were sliced for HPT processing. Prior to HPT processing, the as-cast Zn−3Mg alloy underwent a homogenization heat treatment in a vacuum tube furnace at 360 ± 2 °C for 15 h followed by water quenching. For the HPT alloy samples, 1.5 mm thickness disks were sliced, using a low-speed diamond saw, from the heat-treated Zn−3Mg bar, and slightly polished prior to HPT processing. For the HPT hybrid samples, Zn and Mg disks having thicknesses of 0.665 mm and 0.169 mm, respectively, were sliced using electro-discharge machining, and a set of three disks were stacked on top of each other in the order of Zn/Mg/Zn so that the targeted bulk composition of the resulting HPT hybrid samples was Zn−3Mg. It is important to note that the hybrid, synthesized by the solid-state reaction through HPT, produces a heterostructure in terms of the texture and compositions across the disk diameter [1–10], and thus, the composition is estimated as an average for the entire disk volume.

HPT processing was performed in quasi-constrained conditions [34,35] at RT under an applied pressure of 6 GPa, a constant rotational speed of 1 rpm, and for 30 turns. Fig. 1 provides a schematic of the experimental set-ups used for the fabrication of the HPT alloy and HPT hybrid samples. It should be noted that the temperature rise was monitored during HPT processing, finding a maximum temperature below 50 °C, which is considered insufficient to have any significant effect in the microstructural evolution reported, in agreement with a recent report [36]. After HPT processing, some alloy and hybrid samples were then subjected to PDA at 200 °C for 1 h in a vacuum tube furnace followed by air cooling. HPT-processed disks were cut along their diameter with a low speed diamond saw, and the resulting cross sections were mechanically ground using abrasive SiC papers (MetLab) up to 1200 grit. Specimens were further polished with polycrystalline diamond pastes (MetLab) of 6, 3, 1 and 0.25 μm particle size, sequentially, using velvet polishing cloths (Vel-Lap, MetLab). Final polishing was performed with a colloidal silica suspension of 0.04 μm particle size (OP−S NonDry, Struers) using a neoprene polishing cloth (OP-Chem, Struers). Ethanol was used as a lubricant during polishing, as well as the immersion medium for the ultrasonic cleaning performed between consecutive polishing steps.

2.2. Microstructural characterization

Scanning electron microscopy (SEM), electron backscattered diffraction (EBSD), and energy-dispersive spectroscopy (EDS) were performed in a Tescan Mira3 FEG-SEM at the periphery (less than 1 mm away from the disk edge) of the mid-thickness region of the cross-sectional plane along the diameter of the HPT samples. An accelerating voltage of 25 kV and a working distance of 10 mm were used for SEM image acquisition.

EBSD orientation maps, with an area of ~12 × 12 μm^2, were acquired using a step size of 0.05 μm with an EDAX TSL OIM Data Collection System 7. Dynamic background subtraction was used to obtain Kikuchi patterns with similar intensities. EBSD orientation maps were also acquired for the heat-treated alloy before HPT processing, and in such cases the step size used was 0.5 μm and the area mapped was ~250 × 250 μm^2. The EBSD datasets were analyzed using EDAX TSL OIM Analysis 7, from which inverse pole figure (IPF) maps, kernel average misorientation (KAM) maps, phase maps, grain size distribution plots and misorientation angle plots were obtained. IPF maps were used to generate the (0001) pole figures for Zn and Mg. Clean-up procedures, including neighbor confidence index (CI) correlation and grain dilation, were applied to the as-processed EBSD scans to minimize the number of incorrectly indexed pixels. Grains were identified as any set of at least 10 neighboring pixels having a CI > 0.1 with a misorientation angle lower than 5°. Only points with CI values greater than 0.1 were considered for statistical measurements. KAM maps, including all the pixels with a CI > 0.1, were generated such that misorientation angles up to 3° with their first nearest neighboring pixels were recorded.

EDS elemental point and map analysis was performed on the alloy before and after the heat treatment, as well as in the hybrid after HPT and after HPT + PDA. An accelerating voltage of 6 keV was selected for the EDS elemental maps, which were acquired using the EDAX TEAM system for at least 150 k counts.

Transmission electron microscopy (TEM) and scanning-transmission electron microscopy (STEM) were performed on samples extracted from a plane normal to that used for SEM imaging. Such samples, having dimensions of ~5 × 15 μm^2, were obtained using a standard lift-out technique in a Hitachi NB5000 focused ion beam (FIB-SEM). S/TEM imaging was performed using a FEI Titan aberration-corrected TEM/STEM at 300 kV. Bright field (BF) images and selected area electron diffraction (SAED) patterns

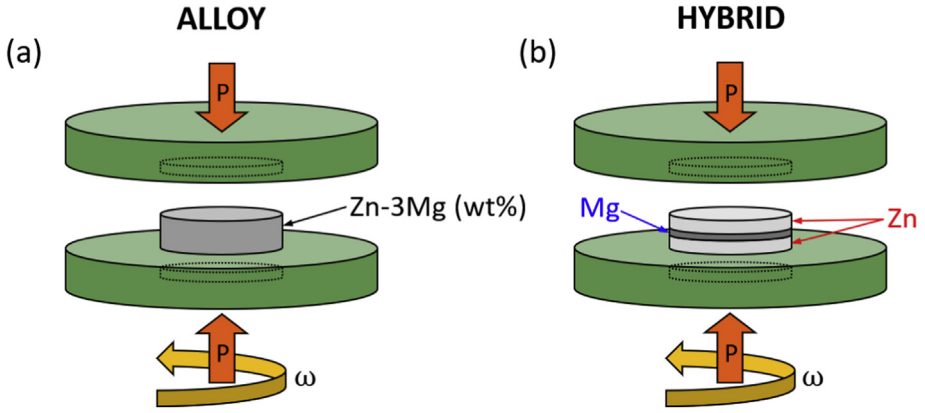

Fig. 1. Experimental set-ups for the fabrication of the HPT-processed (a) alloy and (b) hybrid. P indicates the applied pressure and ω indicates the rotational speed.

were collected in TEM mode, whereas BF and high-angle annular dark field (HAADF) images were acquired in STEM mode. Phase identification via SAED ring pattern analysis was carried out using the ringGUI package of the CrysTBox (Crystallographic Toolbox) open software.

2.3. Micro-mechanical testing

A Clark CM-800AT microhardness tester was used to obtain Vickers microhardness (HV) measurements, which were acquired using a load of 50 gf and a dwell time of 5 s, on the cross-sectional plane along the disk radius of the HPT-processed samples. The HV values were recorded following a rectilinear grid pattern at a uniform incremental spacing of 0.15 mm in the horizontal (radial) and vertical (thickness) directions. The resulting data set was plotted directly, without averaging or any other manipulation, in the form of color-coded contour maps to provide a visual comparison of the distribution and evolution of the hardness values across the disk.

3. Results

3.1. Microstructural evolution of as-cast alloy after heat treatment

Fig. 2 (a) and (b) shows the microstructure of the as-cast Zn−3Mg alloy, where relatively equiaxed structures (see inset in (b)) were heterogeneously dispersed within a fine lamellar eutectic matrix of Zn and Mg_2Zn_{11}. The overall composition of the area depicted in Fig. 2 (c) was determined from EDS mapping, and it is included in Table 1. The chemical composition of the light and dark phases was also investigated through a series of EDS measurements, points 1−6 highlighted in Fig. 2 (c), and their average values are provided in Table 1. Fig. 2 (d) and (e) present the corresponding Zn and Mg EDS elemental maps. The average chemical composition of the relatively equiaxed phases, as measured by EDS, was 5.3 ± 0.3 wt% Mg and 94.7 ± 0.3 wt% Zn (see points 1, 2 and 3 in Fig. 2 (c) and their average composition in Table 1). Because this composition is consistent with that of the Mg_2Zn_{11} phase, the authors believe that the relatively equiaxed phases correspond to larger areas of Mg_2Zn_{11} phase, which are scattered across the lamellar eutectic matrix in the as-cast state. This lack of homogeneity is presumably associated to Mg_2Zn_{11} segregation at low cooling rates, which is consistent with the increase in size of secondary phases and microsegregation reported by Khan et al. [37] at decreasing cooling rates in different Mg alloys.

Fig. 2 (f) and (g) shows the microstructure of the heat-treated Zn−3Mg alloy. The microstructure coarsened and the Mg-rich globular structures were no longer present. The overall composition of the area depicted in Fig. 2 (h) was determined from EDS mapping, and it is included in Table 1. The chemical composition of the light and dark phases was investigated using a series of EDS measurements, see points 1−6 highlighted in Fig. 2 (h), and their average values are provided in Table 1. Fig. 2 (i) and (j) presents the corresponding Zn and Mg EDS elemental maps.

Table 1 presents EDS measurements in locations 1−6 highlighted in Fig. 2 (c) and (h). The darker regions (points 1, 2 and 3) exhibited an average composition of ~94Zn−6Mg, whereas lighter regions (points 4, 5 and 6) revealed an average composition close to 100% Zn.

3.2. Microstructural evolution of heat-treated alloy after HPT and subsequent PDA

Fig. 3 shows a series of TEM/STEM images and SAED patterns corresponding to the ultrafine-grained microstructure obtained in the HPT alloy. As observed in the bright-field BF-TEM image in Fig. 3 (a), the microstructure exhibited grain sizes ranging between ~ 100 and 300 nm.

Fig. 3 (b) shows the corresponding SAED pattern, where the left half is the original pattern and the right half is the processed pattern after beam-stop removal and rotational averaging about its center to eliminate the influence of diffraction ring artifacts due to non-uniform grain size and/or crystal orientation effects [38]. The SAED pattern was calibrated against a known camera length for accurate determination of the d-spacings. A magnified view of the rotationally averaged SAED pattern is shown in Fig. 3 (c) with its corresponding line radial intensity profile, where the labelled peaks correspond to different Bragg reflections. The d-spacings associated with diffraction planes for $2\theta < 100^\circ$ were measured, for peaks having at least 10% maximum intensity, and compared to those of theoretical Zn−Mg phases tabulated in the International Crystalline

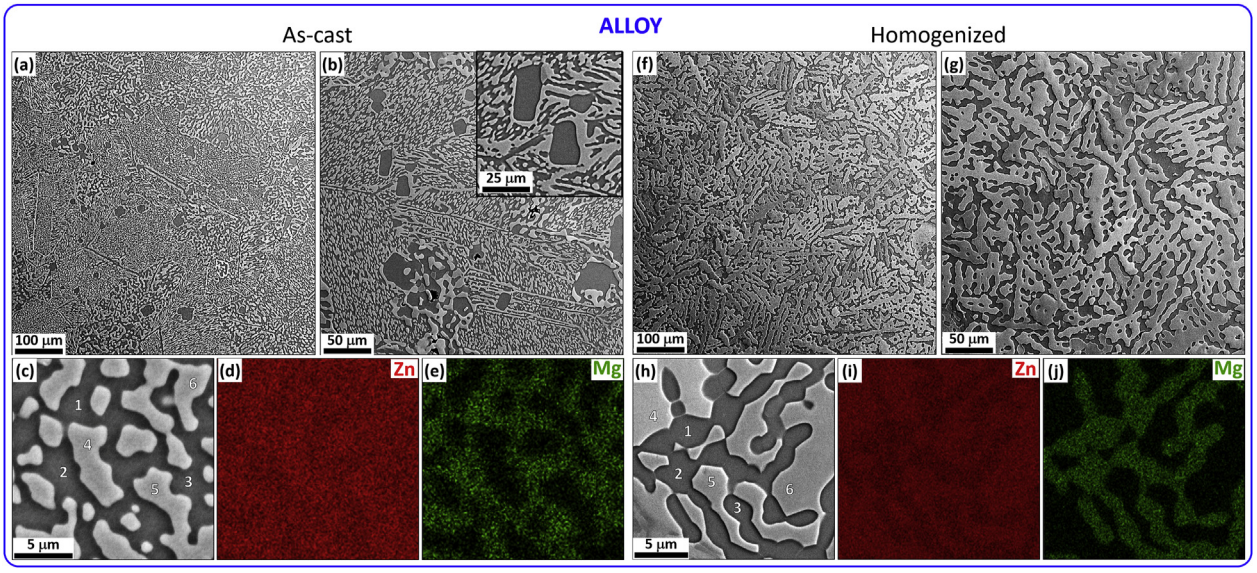

Fig. 2. BSE-SEM photomicrographs and EDS compositional maps of the Zn−3Mg alloy: (a−e) as-cast, (f−j) heat-treated. The points labelled 1−6 in (c) and (h) indicate where EDS analysis was performed.

Table 1
Chemical compositions of the as-cast and heat-treated alloy measured by EDS at different locations in Fig. 2 (c) and (h), respectively.

Condition	Measurement location	Zn		Mg	
		(wt. %)	(at. %)	(wt. %)	(at. %)
As-cast	Whole area	96.7	91.7	3.3	8.3
	Points 1, 2 and 3	94.7 ± 0.3	86.9 ± 0.7	5.3 ± 0.3	13.1 ± 0.7
	Points 4, 5 and 6	100	100	0	0
Heat-treated	Whole area	97.2	92.8	2.8	7.2
	Points 1, 2 and 3	94.2 ± 0.1	85.7 ± 0.3	5.8 ± 0.1	14.3 ± 0.3
	Points 4, 5 and 6	100	100	0	0

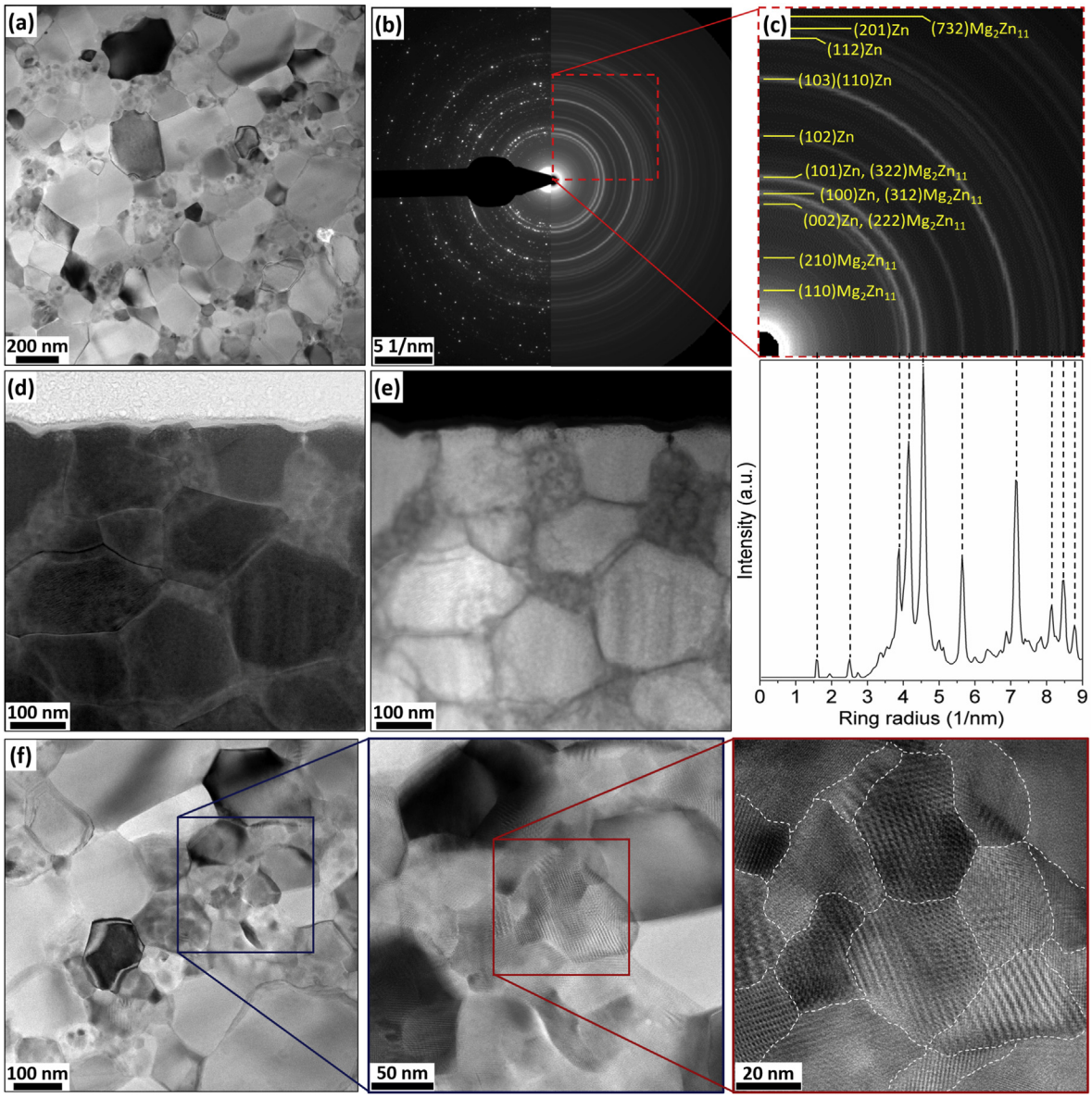

Fig. 3. TEM/STEM images of the HPT alloy at the periphery of the cross section: (a) BF-TEM and (b) corresponding SAED pattern: original pattern (left) and processed pattern (right), (c) region of the SAED pattern where the phases were labelled according to the radial intensity profile, (d) BF-STEM, (e) corresponding HAADF-STEM, (f) HRTEM sequential imaging revealing the presence of nanocrystalline domains (denoted by white dash lines).

Structure Database (ICSD) (#421014 for Zn and #104898 for Mg_2Zn_{11}).

Accordingly, the Zn and Mg_2Zn_{11} phases and their corresponding diffraction planes were labelled in the diffraction rings with (h k l) Miller indices. It is noted that the four peaks with highest intensity were associated with more than one reflection, and that the most intense peak also corresponded to the highest intensity peak in both the Zn and Mg_2Zn_{11} theoretical spectra. No other Zn–Mg phase was a good fit for any of the diffraction rings. The contrast differences in BF and corresponding HAADF-STEM images

in Fig. 3 (d) and (e), respectively, show a heterogeneous distribution of Zn and Mg_2Zn_{11} phases. Because the contrast level in HAADF-STEM imaging mode is directly proportional to the atomic number, the bright grains correspond to Zn, whereas the dark areas correspond to Mg_2Zn_{11}-rich regions.

In addition, nanocrystalline domains (denoted by white dashed lines) are readily apparent in between coarser grains in the HRTEM sequential imaging presented in Fig. 3 (f). Note the presence of Moiré fringe patterns within the nanocrystalline domains, which are characteristic of overlapping lattice reflections. Fast Fourier Transform analysis indicated the presence of Mg_2Zn_{11} and Zn phases. The Moiré fringes visible in Fig. 3 (f) follow rectilinear patterns within adjacent nanocrystalline domains, and did not provide evidence for dislocations.

A BSE SEM photomicrograph of the HPT alloy is shown in Fig. 4 (a), in a viewing plane normal to that of the TEM images provided in Fig. 3. The grains appear to be fairly equiaxed, with an average size of ~200–400 nm. The inset of Fig. 4 (a) shows the darker areas between the neighboring brighter grains, consistent with the TEM observations. It is apparent from Fig. 4 (b) that after PDA the average grain size of the HPT alloy increased to ~ 600–800 nm. The HPT + PDA microstructure exhibited grains of two clear contrast levels, which appear to be free of precipitates in the grain interiors and at the grain boundaries. The area fractions of the light and dark phases, determined using the threshold tool in ImageJ, were 0.59 and 0.41, respectively.

3.3. Microstructural comparison between the alloy and hybrid after HPT and subsequent PDA

The elemental distribution and overall composition of the HPT hybrid and HPT + PDA hybrid was obtained from EDS mapping, and it is depicted in Fig. 5 (a) and (b), respectively. The analysis shows that, for both samples, Zn and Mg were evenly distributed, and that the chemical composition of the areas investigated were close to the targeted Zn–3Mg (wt.%).

Fig. 6 shows a set of maps (image quality, Zn phase, Mg_2Zn_{11} phase and Mg phase) obtained from EBSD analysis for the alloy after (a) heat treatment, (b) HPT, (c) HPT + PDA, and for the hybrid after (d) HPT and (e) HPT + PDA. All the EBSD scans were acquired from the mid-thickness plane of the cross-section of the disk, less than 1 mm away from the edge. The images in Fig. 6 (a), (b) and (c) are comparable to those shown in Figs. 2–4. Despite the relatively low BSE intensity of the Mg_2Zn_{11} phase in comparison to Zn, it was crystallographically identified by EBSD. Due to possible interaction volume effects, phase quantification analysis was not performed. In agreement with the SEM and TEM observations, the EBSD maps showed the grain refinement after HPT and the grain coarsening after subsequent PDA, as observed in Fig. 6 (b) and (c), respectively. This trend was also observed for the HPT hybrids, as evident in Fig. 6 (d) and (e). The Zn, Mg, and Mg_2Zn_{11} structures were identified via EBSD for the hybrid samples.

The grain size (GS) distributions, determined from EBSD analysis after HPT and HPT + PDA, are plotted in Fig. 7 for the alloy (a) and the hybrid (c). After HPT, the GS distributions of the alloy and the hybrid were similar, with an average GS of 213 ± 59 nm and 180 ± 71 nm, respectively. After PDA, the average GS increased to about ~700 nm in the alloy, and to ~400 nm in the hybrid. In both material conditions, the GS range increased after HPT + PDA compared to that after HPT. However, unlike that for the alloy, the GS distribution for the hybrid did not exhibit a unimodal Gaussian profile; it was right-skewed, indicating that a majority of the grains exhibited a larger GS than that of the average. It should be noted that the average GS values were also measured using the linear intercept method from TEM images according to ASTM E112-13 "Standard Test Methods for Determining Average Grain Size", and they were consistent with those reported from EBSD analysis.

The distributions of misorientation angles, within the range 2–93.5°, after HPT and HPT + PDA are displayed in Fig. 7 (b) and (d) for the alloy and the hybrid, respectively. In the alloy, the fractions of misorientation angles, both after HPT and HPT + PDA, follow a similar trend, increasing gradually from 2 to 40°, where the fraction of misorientation angles is always larger after HPT. From 40 to 93.5°, the fraction of misorientation angles decreased consistently for increasing values after HPT, whereas it remained fairly uniform for the HPT + PDA condition. In the hybrid, the trends exhibited by the misorientation angle distributions after HPT and HPT + PDA were significantly different. After HPT, there were ~15% of low angle boundaries (LABs) (<15° misorientation) in the microstructure, whereas that value was less than 7% after HPT + PDA. Thus, the fraction of high angle boundaries (HABs) (>15° misorientation) was higher after PDA. In both material conditions, the fraction of misorientation angles increases in the range 10–30° and decreases in the range 30–70°. The regions gathering the most frequently occurring misorientation angles were 20–40° after HPT and 75-93.5° after HPT + PDA.

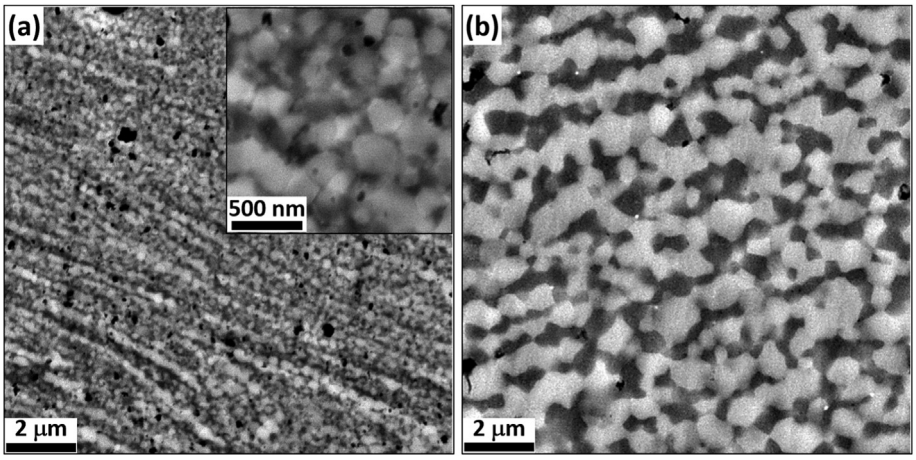

Fig. 4. BSE-SEM images of the (a) HPT alloy and (b) HPT + PDA alloy at the periphery of the cross section. The image inset corresponds to a magnified view of the same microstructure.

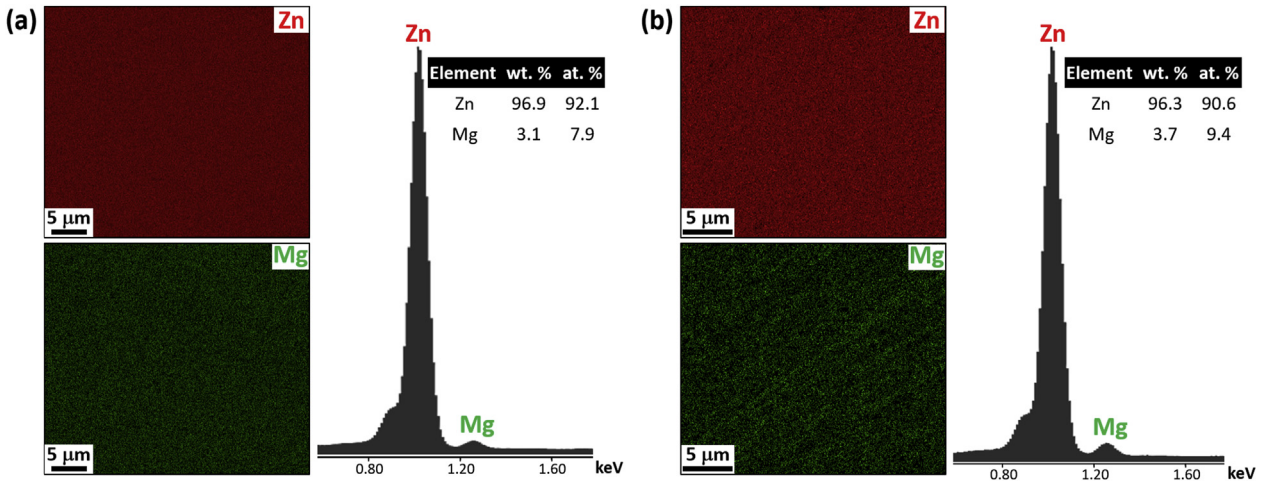

Fig. 5. EDS elemental maps of the (a) HPT hybrid and (b) HPT + PDA hybrid at the periphery of the cross section. Their corresponding EDS spectra and chemical composition are also provided.

3.4. Microhardness comparison between the alloy and hybrid after HPT and subsequent PDA

The distribution of Vickers microhardness (HV) was examined over the radial cross-section of the alloy and hybrid after HPT and HPT + PDA, and the data is presented in color-coded contour maps in Fig. 8. The HV values are indicated in the color key scale on the bottom right. The hardness value of the heat-treated alloy before HPT was 109 HV, and the HPT processing significantly increased the hardness, see Fig. 8 (a). However, the HV values for the alloy did not change dramatically across the radius of the samples after HPT and HPT + PDA. The average hardness values are 139 HV and 136 HV, before and after PDA, respectively. However, it was observed that hardness was slighlty less homogenous after PDA. The "softer" region indicated by green tones expands from $r < 1$ mm after HPT to $r < 2$ mm after PDA. Also, the maximum HV values near the disk edge at $r > 4$ mm increase slightly from ~150 HV after HPT to ~155 HV after PDA.

The hardness of the hybrid varied significantly across the radius both after HPT and HPT + PDA, as observed in Fig. 8 (b). The average HV values were comparable to those of the alloy: 133 HV and 138 HV before and after PDA, respectively. The highest hardness values were found at $2 < r < 4$ mm, with maximum values ~230 HV and ~250 HV after HPT and HPT + PDA, respectively. It is noted that the outermost peripheral region of the hybrid samples, at $r > 4$ mm, presents lower hardness values both after HPT and HPT + PDA.

4. Discussion

4.1. Effect of heat treatment on the microstructure of the as-cast alloy

As observed in Fig. 2, the heat treatment was effective in dissolving the Mg-rich globules in the as-cast state, providing a more interconnected and homogenous microstructure. As depicted in Table 1, the compositions of the darker regions in the microstructure before and after heat treatment, shown in Fig. 2 (c) and (h), respectively, are in good agreement with that of the Mg_2Zn_{11} intermetallic phase: 93.7Zn-6.3 Mg. This indicates that the investigated alloy, with an overall composition of 97Zn−3Mg, consists of an eutectic mixture of Zn and Mg_2Zn_{11}. A slight increase in Mg concentration of the darker regions after heat treatment was observed in Table 1, suggesting that the composition of the Mg_2Zn_{11} phase after heat treatment was closer to its theoretical composition. This is consistent with the experimentally-observed dissolution of the Mg-rich globules that formed after casting. Thereby, the heat treatment was expected to have promoted atomic diffusion, such that the Mg atoms enriched the Mg_2Zn_{11} phase, providing a condition closer to equilibrium.

4.2. Microstructural evolution of heat-treated alloy after HPT and subsequent PDA

As observed in Fig. 3 (a), the microstructure of the alloy after HPT processing consists of a matrix of grains with sizes ranging between ~ 100 and 300 nm. The uniform contrast level of larger grains may indicate that they correspond to dislocation-free single-phase grains that underwent dynamic recrystallization during HPT processing. On the other hand, the varying contrast levels observed in the smaller grains may suggest the presence of nanoscale intermetallic phases responsible for the impingement of their grain boundaries. Analysis of the SAED pattern in Fig. 3 (b) and (c) confirmed that the microstructure consisted of a mixture of Zn and Mg_2Zn_{11}, suggesting that no additional phase formed during HPT processing. It is worth highlighting that HPT processing of the hybrid under the same conditions resulted in the formation of Mg_2Zn_{11} and $MgZn_2$ intermetallic compounds.

The contrast differences across the HAADF-STEM image in Fig. 3 (e) indicated that the bright and dark areas were associated with Zn and Mg_2Zn_{11}, respectively. The larger grains with a more uniform contrast correspond to Zn, whereas the larger dark areas with non-uniform contrast are suggested to be clusters of nanosized Mg_2Zn_{11} intermetallic phases. Alternatively, it is also possible that the non-uniform contrast within the darker areas in Fig. 3 (e) corresponds to dislocation networks inside Mg_2Zn_{11} grains. Note that dislocation arrays should appear bright in HAADF mode. Therefore, dislocations may also be present inside larger Zn grains, but not visible due to the higher Z contrast of Zn in HAADF mode as compared to Mg_2Zn_{11}. In addition, the darker appearance of the grain boundaries may indicate grain boundary segregation of the Mg_2Zn_{11} phase during HPT processing. The HRTEM images presented in Fig. 3 (f) confirmed the presence of nanocrystalline domains. These observations are consistent with those obtained from the cross-sectional plane through BSE-SEM imaging in Fig. 4 (a).

Upon PDA, the average GS of the alloy increased to ~600−800 nm, and its microstructure appeared to be precipitate-

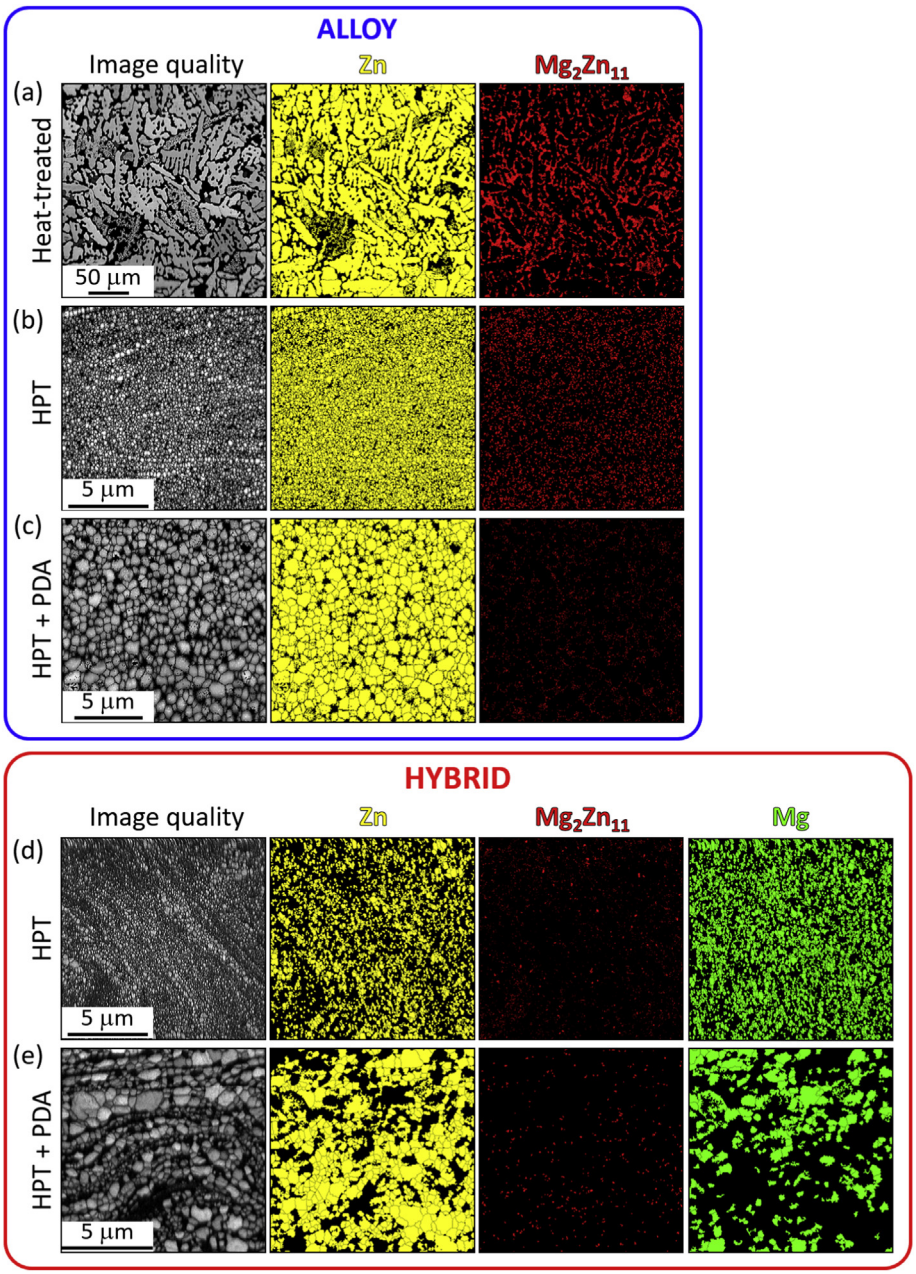

Fig. 6. EBSD phase maps taken at the periphery of the cross section in the alloy after (a) heat treatment, (b) HPT and (c) HPT + PDA; and in the hybrid after (d) HPT and (e) HPT + PDA.

free, as observed in Fig. 4 (b). This may indicate that the Mg_2Zn_{11} nanoscale intermetallics, which were either clustered between neighboring Zn grains, or located along the grain boundaries after HPT, diffused during PDA and presumably coalesced into larger grains. This would lead to a decrease of Mg_2Zn_{11} surface area, resulting in a more energetically favorable condition closer to equilibrium, which is consistent with the microstructure exhibited in Fig. 4 (b). The area fractions of Zn and Mg_2Zn_{11} were estimated as 0.59 and 0.41, respectively, which are reasonably close to the theoretical equilibrium composition of 57Zn–43Mg_2Zn_{11} for Zn–3Mg.

4.3. Microstructural comparison between the alloy and hybrid after HPT and subsequent PDA

Both Zn and Mg_2Zn_{11} were found in the alloy and its hybrid counterpart after HPT and PDA. In addition, the Mg phase was also identified in the hybrid. According to the EBSD phase maps in Fig. 6, the amount of Mg in the inspected region appears to be significantly greater than the 3 wt% intended in the bulk composition. This may be explained as follows. First, there is a preferential distribution of Mg towards the regions of higher plastic deformation

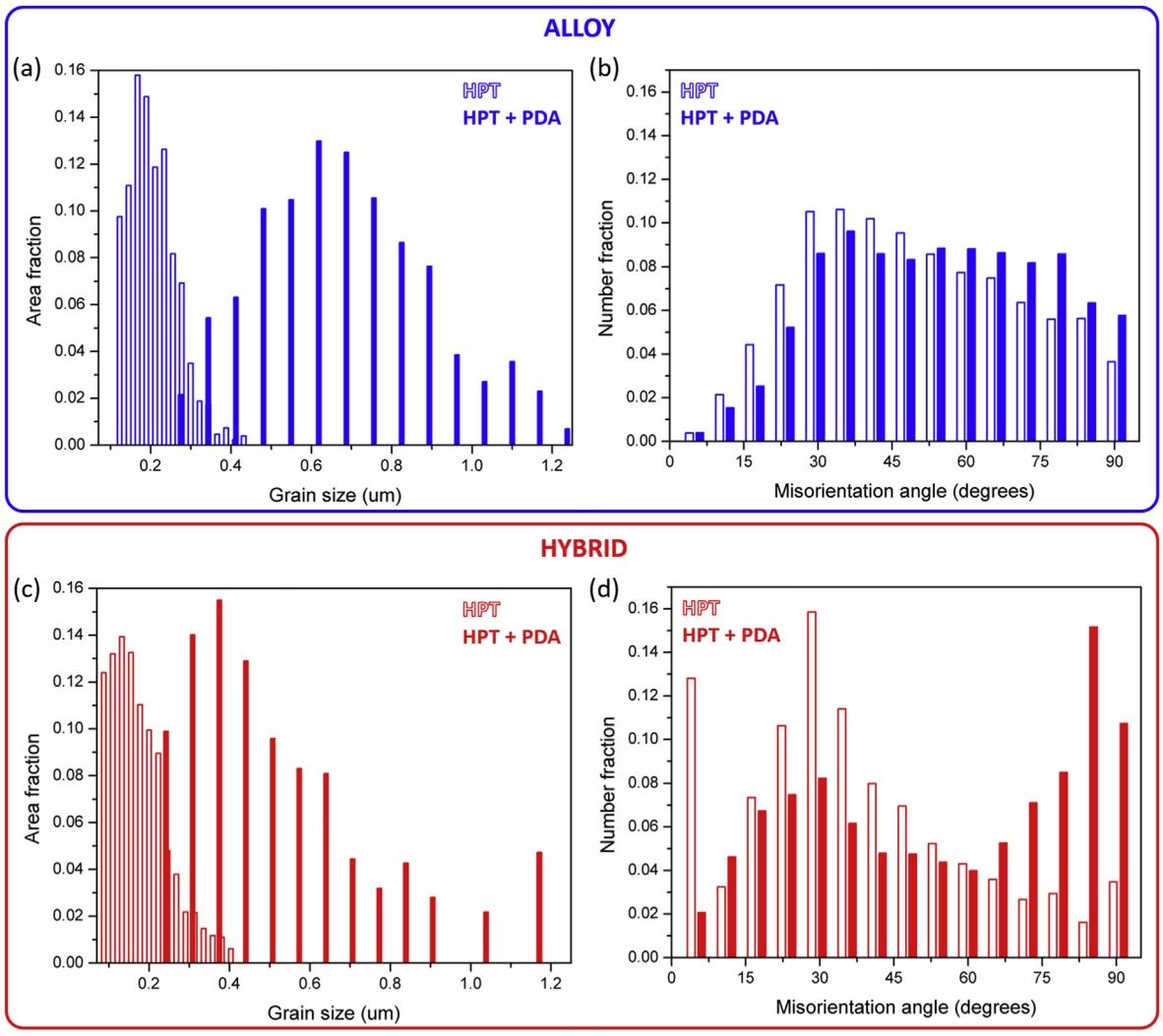

Fig. 7. EBSD grain size and misorientation angle plots for the (a)–(b) alloy and (c)–(d) hybrid after HPT and HPT + PDA.

(i.e. disk periphery), where Mg_2Zn_{11} intermetallic phases are more likely to be formed during HPT processing. This has been consistently reported in HPT hybrids of different compositions [1,2,4–9]. Second, the mid-thickness region of the cross-sectional sample, where the EBSD map was acquired, corresponds to the location of the original Mg disk in the hybrid sample. Thus, despite the phase mixing and atomic diffusion taking place during HPT, the mid-thickness location may still be more likely to be Mg-rich, which is consistent with the different levels of phase transformation reported recently in a HPT-processed Ti–Al alloy [39]. These two factors indicate that the overall composition of the HPT hybrids is far from uniform across the disk samples. It is noted that the $MgZn_2$ intermetallic phase found in the hybrid after HPT and subsequent PDA processing was not indexed in EBSD analysis, which is likely because it has the same crystal structure as Zn and Mg, which were preferentially chosen by the EBSD software.

Regarding the grain refinement, HPT processing was equally effective in refining the GS of the alloy and the hybrid to ~200 nm. However, despite a GS increase in both material conditions after subsequent PDA, the alloy exhibited a larger average GS (~700 nm), compared to that of the hybrid (~400 nm). This may be rationalized by the distinct microstructural features exhibited in the alloy and the hybrid after equivalent HPT + PDA processing. The alloy exhibited precipitate-free Zn and Mg_2Zn_{11} grains, with a wide range of GS, that were uniformly distributed in the microstructure, which is consistent with the Gaussian distribution profile depicted in Fig. 7 (a). In contrast, the hybrid presented a matrix of Zn grains with finer neighboring Mg-rich grains, where the Mg_2Zn_{11} and $MgZn_2$ intermetallic precipitates were segregated, limiting their GS increase [8]. Moreover, this multimodal distribution of ultrafine grains and dislocation-free coarse grains was suggested to be responsible for the simultaneous increase of hardness and strain rate sensitivity in the Zn–3Mg hybrid after PDA [8]. It is worth mentioning that HPT-processed pure Zn [14] and Mg [18] exhibited an average GS of ~5.2 μm and ~1 μm, respectively, at the steady-state regime. Thus, HPT processing of Zn–3Mg, either in the alloy or hybrid form, results in more severe grain refinement than their base materials.

With respect to the distribution of misorientation angles, it is noted that there were large fractions of HABs found in both the alloy and the hybrid, and this is suggested to be due to the evolution of LABs into HABs due to the dynamic recrystallization which occurred during HPT. The observed peak at ~30° in the misorientation distribution angle is attributed to the strong basal fiber texture developed in Zn and Mg during HPT processing, as observed in Fig. 9 (a), (c) and (d), which is consistent with previous studies [7,20,40]. The fraction of misorientation angles at ~30° decreased significantly in the hybrid after subsequent PDA, which was due to a

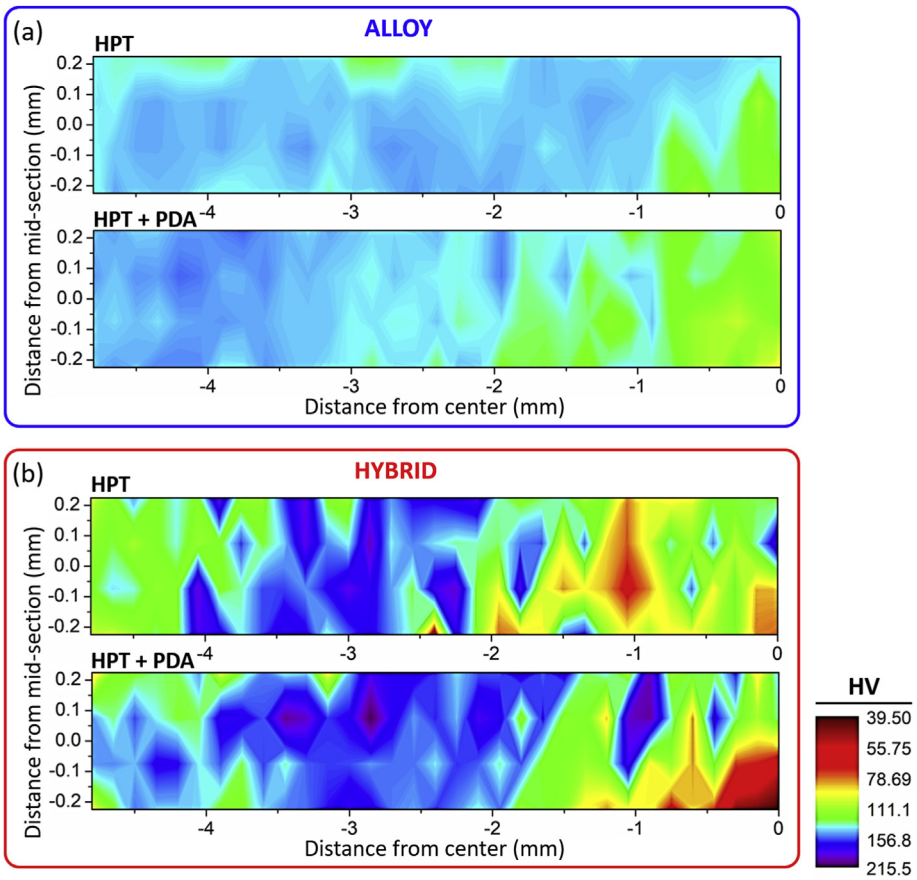

Fig. 8. Color-coded Vickers microhardness (HV) contour maps for the (a) alloy and (b) hybrid after HPT and HPT + PDA. (For interpretation of the references to color in this figure legend, the reader is referred to the Web version of this article.)

weakening of the basal texture, as observed in Fig. 9 (e) and (f). Note that after PDA, the majority of the basal poles in the hybrid, both in the Zn and Mg phases, are tilted away from the {0001} normal, indicating a reorientation of the crystals. Zeng et al. [41] also showed a deviation of the basal poles away from its normal direction in the {0001} pole figure after annealing a Mg–Zn alloy, which is consistent with the current observations. The maximum texture intensity (I_{max}) of the Mg phase in the hybrid after PDA was notably greater than that of the Zn phase, as there was a larger fraction of poles tilted away from the {0001} normal. This suggests that the Mg phase has a greater influence in the basal texture weakening of the hybrid after PDA. Accordingly, as observed in Fig. 7 (d), the PDA treatment in the hybrid led to a shift of the misorientation angles towards higher values, exhibiting a peak at ~ 90°, which is in good agreement with that of the Mackenzie misorientation distribution for a randomly oriented hexagonal crystal [42].

Fig. 10 illustrates kernel average misorientation (KAM) maps for the alloy and hybrid after HPT and HPT + PDA. The largest orientation gradients in the alloy after PDA are typically observed near the grain boundaries (see inset in Fig. 10 (b)). This supports the hypothesis that the presence of nanosized Mg_2Zn_{11} domains along the grain boundaries is expected to create localized strain gradients in the microstructure. However, the hybrid after PDA exhibited the highest orientation gradients among the four microstructures, as indicated by the amount of green-yellow areas in Fig. 10 (d). Larger grains tended to exhibit orientation gradients near their grain boundaries, whereas smaller grains typically presented more uniform and higher misorientation angles. The misorientation distribution in the hybrid after PDA could result in localized strains, and thus, be somewhat responsible for creating the heterostructure presented earlier [8], which consists of segregated Mg_2Zn_{11} and $MgZn_2$ intermetallics surrounding the finer Mg-rich grains after PDA, which prevents their grain growth during annealing.

The GS distribution, misorientation distribution and texture were similar for both the HPT processed alloy and hybrid. However, the PDA treatment affected the alloy and hybrid differently. The average GS became slightly larger and more uniform in the alloy than in the hybrid, as indicated by Fig. 7 (a) and (c) and observed in Fig. 9 (b) and (d), respectively. The basal texture developed after HPT in both material conditions was maintained after PDA in the alloy, whereas it decreased in the hybrid, which might be related to mechanical anisotropy. In addition, the local misorientations observed in Fig. 10 (b) and (d) for the alloy and hybrid, respectively, could be indicative of the strain gradients created from the precipitation of the nanosized Mg_2Zn_{11} and $MgZn_2$ intermetallic compounds, which may have played an important role in the final mechanical properties.

4.4. Microhardness comparison between the alloy and hybrid after HPT and subsequent PDA

Despite the microstructural similarities between the alloy and the hybrid after HPT processing in terms of GS distribution and texture, Fig. 8 shows that there were notable differences regarding the microhardness distribution. The hybrid exhibited significantly higher HV values, but they were less homogenously distributed across the sample diameter than the alloy. This suggests that the

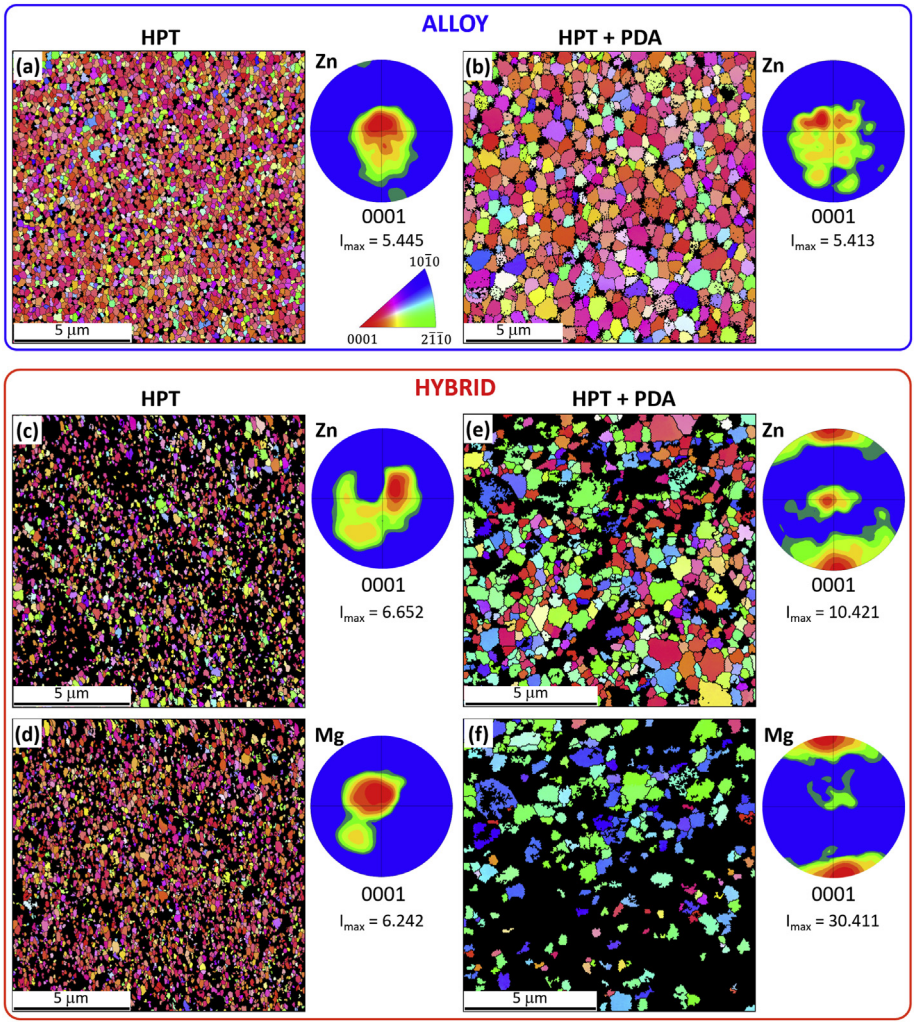

Fig. 9. IPF EBSD maps taken at the periphery of the cross section in the alloy after (a) HPT, (b) HPT + PDA, and in the hybrid after (c and d) HPT and (e and f) HPT + PDA. The {0001} pole figures corresponding to the hexagonal crystal phases identified (Zn and Mg) are provided next to the IPF map.

formation and distribution of the Mg_2Zn_{11} and $MgZn_2$ intermetallic nanoprecipitates during HPT may play a major role. Even though the average HV value of the alloy and the hybrid after HPT were similar, the hybrid hardened significantly more than the alloy during HPT compared to the original hardness of their base materials. The heat-treated Zn−3Mg alloy exhibited an average hardness of 109 HV, whereas that of the pure Zn and Mg were 37 HV and 35 HV, respectively [43,44].

Both the alloy and the hybrid exhibited lower HV values close to the disk center, at $r < 1$ mm, as this region experienced the lowest plastic deformation. In the alloy, the hardness increases gradually from the center to the periphery of the disk, and the gradient became slightly larger after PDA. This is in agreement with the strain hardening model proposed for HPT-processed materials [45]. However, unlike that in the alloy, the outermost peripheral region of the hybrid, at $r > 4$ mm, does not present the highest HV values. This might be due to an increased deformation-induced recrystallization rate in the regions with highest deformation, as reported elsewhere [46]. Consequently, the intermediate regions of the hybrid, at $4 > r > 2$ mm, both after HPT and PDA, which exhibited fine grain sizes and intermetallic precipitates, provided the highest hardness values.

For the hybrid, PDA resulted in an increase in the HV values both at the peripheral and mid-central region and a slight decrease of HV values in the central region, leading to an increase in the microhardness heterogeneity as compared to the HPT condition. Strain softening in the peripheral region of hybrid was associated with the increase in average GS and loss of basal texture after PDA, as observed in Fig. 9. It should also be mentioned that strain softening has previously been reported in pure Zn [14] and Mg [18] during HPT-processing, resulting in a relatively constant hardness level at high strains, which was attributed to the their relatively high homologous temperatures. However, unlike most pure metals and alloys, the hardness of the hybrid does not reach a saturation level after HPT nor subsequent PDA.

Relationships between the microstructural heterogeneities and the micro-mechanical responses in the Zn−3Mg hybrid system have been recently described [8]. A hardenability exponent (η) of 0.535 was reported in the hybrid after HPT, which was the highest η value reported to date, and one order of magnitude larger than most η values reported for HPT-processed alloys [8]. Following the same approach, the degree of strain hardening of the alloy after HPT and HPT + PDA was estimated through the η value, calculated as defined elsewhere [21]. Fig. 11 shows that $\eta = 0.017$ after HPT, and $\eta = 0.056$ after HPT + PDA, which are in agreement with other HPT-processed alloys [21,23,47]. The increased hardenability exponent after PDA is in agreement with the higher hardness heterogeneity observed in Fig. 8 (a) after PDA.

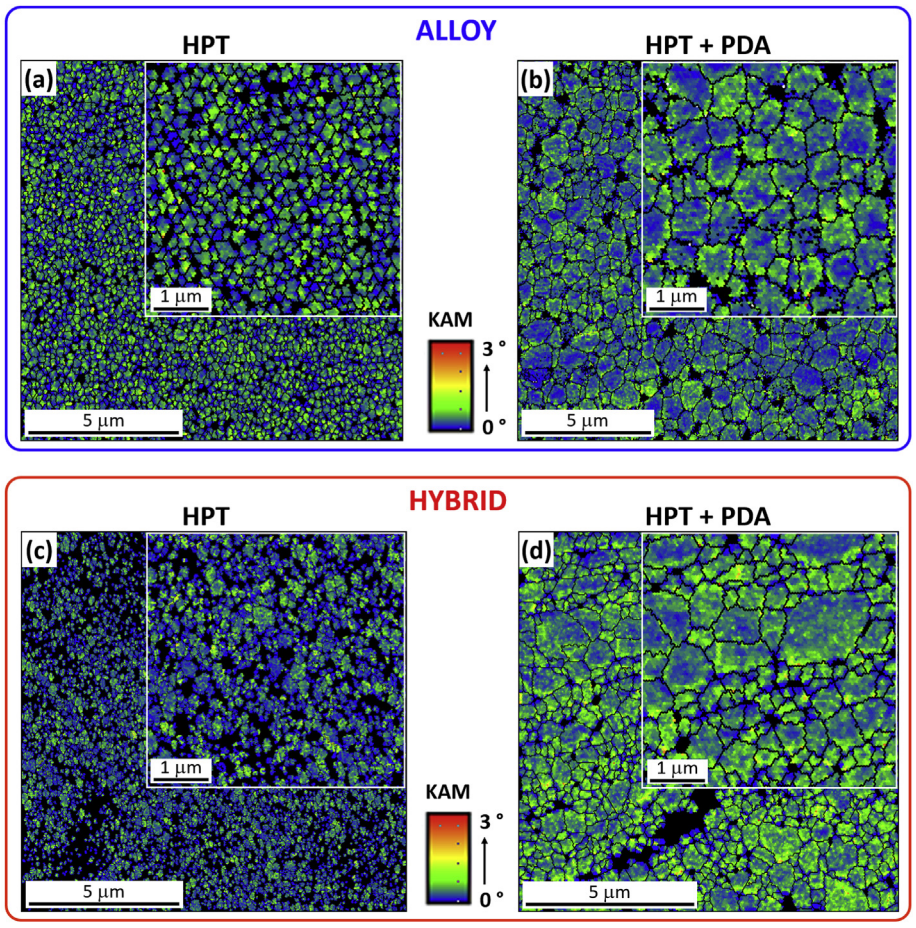

Fig. 10. KAM EBSD maps taken at the periphery of the cross section in the alloy after (a) HPT, (b) HPT + PDA, and in the hybrid after (c) HPT and (c) HPT + PDA. The insets in the top-right corner of the images indicate higher magnification regions of the same areas.

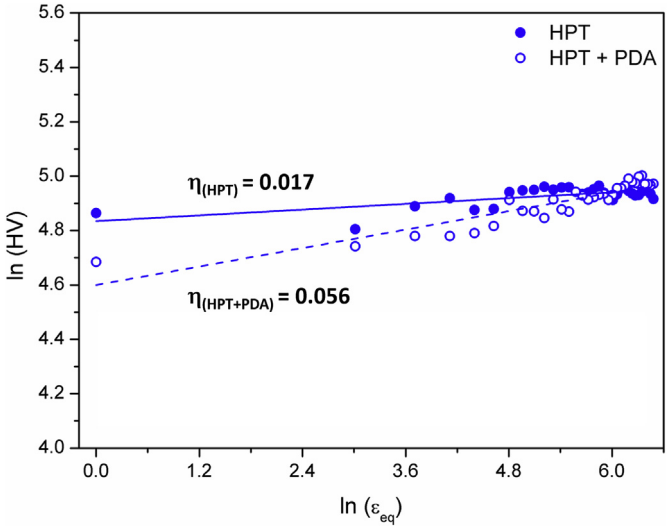

Fig. 11. Double-natural logarithm plots of Vickers hardness (HV) vs. equivalent strain (ε_{eq}) for the alloy after HPT and HPT + PDA. The slope of the linear regresion indicates the hardenability exponent (η).

HPT has a significant impact on the final microhardness of the alloy and the hybrid. The hybrid exhibited an exceptional strain hardening capability as compared to the alloy, however, its HV values were not uniformly distributed across the disk. Instead, the alloy exhibited a notably lower overall hardness, but its HV values were more uniformly distributed along the cross-section. The PDA treatment increased the hardness at the mid-central and periphery regions, but slightly decreased the hardness at the central region, resulting in a more heterogeneous hardness distribution.

5. Summary and conclusions

1. A cast Zn−3Mg (wt.%) alloy and its hybrid counterpart (series of Zn/Mg/Zn disks) were synthesized using quasi-constrained HPT processing at 6 GPa and 1 rpm for 30 turns. Their microstructural and microhardness evolution after HPT and subsequent PDA (200 °C for 1 h + air cooling) was investigated and compared through SEM and TEM/STEM imaging, EDS and EBSD analysis, and Vickers hardness testing.
2. Heat treatment (360 °C for 15 h + water quenching) of the as-cast Zn−3Mg alloy was effective in dissolving the Mg-rich globular phases and providing a more uniform lamellar eutectic microstructure consisting of Zn and Mg_2Zn_{11}.
3. Both the alloy and the hybrid exhibited a similar average GS of ~200 nm after HPT processing, which increased to ~700 nm and ~400 nm, respectively, after PDA. Nanocrystalline Mg_2Zn_{11} domains, which were observed both between the neighboring precipitate-free Zn grains and at the grain boundaries of the alloy after HPT, were believed to coalesce into larger grains maintaining a unimodal GS distribution after PDA.

4. Unlike the alloy, the hybrid after PDA displayed a microstructure consisting of ultrafine Mg-rich grains with sizes of ~300 nm containing $MgZn_2$ and Mg_2Zn_{11} nanoscale precipitates, in a matrix of coarse dislocation-free Zn grains ranging between ~600 and 900 nm. KAM maps of the hybrid after PDA exhibited the largest orientation gradients, mainly in the smaller grains, presumably due to localized strains associated with the intermetallic nanoprecipitates.
5. Basal texture was observed after HPT in the alloy and the hybrid, and this texture was only maintained in the alloy after PDA. Instead, the hybrid presented a more random crystal orientation after PDA in agreement with a peak shift in the misorientation angle plot from ~30° to ~90°. The fractions of LABs and HABs did not change significantly in either material condition before and after PDA.
6. Although the hardness values in the alloy were lower than in the hybrid, they were more uniformly distributed. The PDA treatment resulted in a hardness increase in both material conditions, with maximum values of ~155 HV and ~250 HV near the disk periphery in the alloy and the hybrid, respectively. This in turn increased the hardness heterogeneity, which was notably larger in the hybrid, in agreement with an increase in the hardenability exponent after PDA.

Declaration of competing interest

The authors declare that they have no known competing financial interests or personal relationships that could have appeared to influence the work reported in this paper.

CRediT authorship contribution statement

David Hernández-Escobar: Investigation, Formal analysis, Writing - original draft, Writing - review & editing. **Raymond R. Unocic:** Conceptualization, Investigation, Writing - review & editing. **Megumi Kawasaki:** Conceptualization, Resources, Writing - review & editing. **Carl J. Boehlert:** Conceptualization, Project administration, Supervision, Writing - review & editing.

Acknowledgements

The funding for this research was supported by the National Science Foundation Division of Material Research, under Grant No. DMR-1607942 through the Metals and Metallic Nanostructures (MMN) program (DHE & CJB) and under Grant No. DMR-1810343 (MK). A portion of this research (S/TEM) was conducted at Oak Ridge National Laboratory's Center for Nanophase Materials Sciences (CNMS), a U.S. Department of Energy Office of Science User Facility.

References

[1] K. Oh-ishi, K. Edalati, H.S. Kim, K. Hono, Z. Horita, High-pressure torsion for enhanced atomic diffusion and promoting solid-state reactions in the aluminum–copper system, Acta Mater. 61 (2013) 3482–3489, https://doi.org/10.1016/J.ACTAMAT.2013.02.042.
[2] J.-K. Han, D.K. Han, G.Y. Liang, J.-I. Jang, T.G. Langdon, M. Kawasaki, Direct bonding of aluminum-copper metals through high-pressure torsion processing, Adv. Eng. Mater. 20 (2018) 1800642, https://doi.org/10.1002/adem.201800642.
[3] V.N. Danilenko, S.N. Sergeev, J.A. Baimova, G.F. Korznikova, K.S. Nazarov, R.K. Khisamov, A.M. Glezer, R.R. Mulyukov, An approach for fabrication of Al-Cu composite by high pressure torsion, Mater. Lett. 236 (2019) 51–55, https://doi.org/10.1016/j.matlet.2018.09.158.
[4] M. Kawasaki, B. Ahn, H. Lee, A.P. Zhilyaev, T.G. Langdon, Using high-pressure torsion to process an aluminum–magnesium nanocomposite through diffusion bonding, J. Mater. Res. 31 (2016) 88–99, https://doi.org/10.1557/jmr.2015.257.
[5] J.K. Han, H.J. Lee, J. il Jang, M. Kawasaki, T.G. Langdon, Micro-mechanical and tribological properties of aluminum-magnesium nanocomposites processed by high-pressure torsion, Mater. Sci. Eng. 684 (2017) 318–327, https://doi.org/10.1016/j.msea.2016.12.067.
[6] M. Kawasaki, J.-K. Han, D.-H. Lee, J. Jang, T.G. Langdon, Fabrication of nanocomposites through diffusion bonding under high-pressure torsion, J. Mater. Res. (2018) 1–11, https://doi.org/10.1557/jmr.2018.205.
[7] D. Hernández-Escobar, Z.U. Rahman, H. Yilmazer, M. Kawasaki, C.J. Boehlert, Microstructural evolution and intermetallic formation in Zn Mg hybrids processed by High Pressure Torsion, Philos. Mag. A 99 (2019) 557–584, https://doi.org/10.1080/14786435.2018.1546962.
[8] D. Hernández-Escobar, J. Marcus, J.-K. Han, R.R. Unocic, M. Kawasaki, C.J. Boehlert, Effect of post-deformation annealing on the microstructure and micro-mechanical behavior of Zn–Mg hybrids processed by High-Pressure Torsion, Mater. Sci. Eng. (2019) 138578, https://doi.org/10.1016/j.msea.2019.138578.
[9] N. Ibrahim, M. Peterlechner, F. Emeis, M. Wegner, S.V. Divinski, G. Wilde, Mechanical alloying via high-pressure torsion of the immiscible Cu50Ta50 system, Mater. Sci. Eng. 685 (2017) 19–30, https://doi.org/10.1016/j.msea.2016.12.106.
[10] Y. Qi, A. Kosinova, A.R. Kilmametov, B.B. Straumal, E. Rabkin, Plastic flow and microstructural instabilities during high-pressure torsion of Cu/ZnO composites, Mater. Char. 145 (2018) 389–401, https://doi.org/10.1016/j.matchar.2018.09.001.
[11] R.Z. Valiev, R.K. Islamgaliev, I.V. Alexandrov, Bulk nanostructured materials from severe plastic deformation, Prog. Mater. Sci. 45 (2000) 103–189, https://doi.org/10.1016/S0079-6425(99)00007-9.
[12] J.-K. Han, J. Jang, T.G. Langdon, M. Kawasaki, Bulk-state reactions and improving the mechanical properties of metals through high-pressure torsion, Mater. Trans. 60 (2019) 1131–1138, https://doi.org/10.2320/matertrans.MF201908.
[13] K. Edalati, Z. Horita, High-pressure torsion of pure metals: influence of atomic bond parameters and stacking fault energy on grain size and correlation with hardness, Acta Mater. 59 (2011) 6831–6836, https://doi.org/10.1016/j.actamat.2011.07.046.
[14] K. Edalati, Z. Horita, Significance of homologous temperature in softening behavior and grain size of pure metals processed by high-pressure torsion, Mater. Sci. Eng. 528 (2011) 7514–7523, https://doi.org/10.1016/j.msea.2011.06.080.
[15] N. Maury, N.X. Zhang, Y. Huang, A.P. Zhilyaev, T.G. Langdon, A critical examination of pure tantalum processed by high-pressure torsion, Mater. Sci. Eng. 638 (2015) 174–182, https://doi.org/10.1016/J.MSEA.2015.04.053.
[16] Y. Ito, Z. Horita, Microstructural evolution in pure aluminum processed by high-pressure torsion, Mater. Sci. Eng. 503 (2009) 32–36, https://doi.org/10.1016/J.MSEA.2008.03.055.
[17] A.P. Zhilyaev, S. Lee, G. V Nurislamova, R.Z. Valiev, T.G. Langdon, Microhardness and microstructural evolution in pure nickel during high-pressure, Torsion 44 (2001) 2753–2758.
[18] K. Edalati, A. Yamamoto, Z. Horita, T. Ishihara, High-pressure torsion of pure magnesium: evolution of mechanical properties, microstructures and hydrogen storage capacity with equivalent strain, Scripta Mater. 64 (2011) 880–883, https://doi.org/10.1016/j.scriptamat.2011.01.023.
[19] K. Edalati, E. Matsubara, Z. Horita, Processing pure Ti by high-pressure torsion in wide ranges of pressures and strain, Metall. Mater. Trans. 40 (2009) 2079–2086, https://doi.org/10.1007/s11661-009-9890-5.
[20] B. Srinivasarao, A.P. Zhilyaev, T.G. Langdon, M.T. Pérez-Prado, On the relation between the microstructure and the mechanical behavior of pure Zn processed by high pressure torsion, Mater. Sci. Eng. 562 (2013) 196–202, https://doi.org/10.1016/j.msea.2012.11.027.
[21] Y.C. Wang, T.G. Langdon, Effect of heat treatment on microstructure and microhardness evolution in a Ti–6Al–4V alloy processed by high-pressure torsion, J. Mater. Sci. 48 (2013) 4646–4652, https://doi.org/10.1007/s10853-012-7071-1.
[22] K. Bryła, J. Morgiel, M. Faryna, K. Edalati, Z. Horita, Effect of high-pressure torsion on grain refinement, strength enhancement and uniform ductility of EZ magnesium alloy, Mater. Lett. 212 (2018) 323–326, https://doi.org/10.1016/J.MATLET.2017.10.113.
[23] S.A. Torbati-Sarraf, S. Sabbaghianrad, R.B. Figueiredo, T.G. Langdon, Orientation imaging microscopy and microhardness in a ZK60 magnesium alloy processed by high-pressure torsion, J. Alloys Compd. 712 (2017) 185–193, https://doi.org/10.1016/J.JALLCOM.2017.04.054.
[24] A. Loucif, R.B. Figueiredo, M. Kawasaki, T. Baudin, F. Brisset, R. Chemam, T.G. Langdon, Effect of aging on microstructural development in an Al–Mg–Si alloy processed by high-pressure torsion, J. Mater. Sci. 47 (2012) 7815–7820, https://doi.org/10.1007/s10853-012-6400-8.
[25] K. Edalati, Y. Yokoyama, Z. Horita, High-pressure torsion of machining chips and bulk discs of amorphous Zr50Cu30Al10Ni10, Mater. Trans. 51 (2010) 23–26, https://doi.org/10.2320/matertrans.MB200914.
[26] A.P. Zhilyaev, A.A. Gimazov, G.I. Raab, T.G. Langdon, Using high-pressure torsion for the cold-consolidation of copper chips produced by machining, Mater. Sci. Eng. 486 (2008) 123–126, https://doi.org/10.1016/j.msea.2007.08.070.
[27] M. Khajouei-Nezhad, M.H. Paydar, M. Mokarizadeh Haghighi Shirazi, J. Gubicza, Microstructure and tensile behavior of Al7075/Al composites

consolidated from machining chips using HPT: a way of solid-state recycling, Met. Mater. Int. (2019), https://doi.org/10.1007/s12540-019-00428-7.
[28] P. Straumal, N. Martynenko, A. Kilmametov, A. Nekrasov, B. Baretzky, Microstructure, microhardness and corrosion resistance of WE43 alloy based composites after high-pressure torsion, Materials 12 (2019) 2980, https://doi.org/10.3390/ma12182980.
[29] M. Liu, R. Zheng, C. Ma, N. Tsuji, Ultra-strong, ductile and thermally stable ultrafine grained 5083 Al alloy fabricated by high pressure torsion using pre-sintered powders, Materialia 8 (2019) 100448, https://doi.org/10.1016/j.mtla.2019.100448.
[30] V.V. Stolyarov, Y.T. Zhu, T.C. Lowe, R.K. Islamgaliev, R.Z. Valiev, Processing nanocrystalline Ti and its nanocomposites from micrometer-sized Ti powder using high pressure torsion, Mater. Sci. Eng. 282 (2000) 78–85, https://doi.org/10.1016/S0921-5093(99)00764-9.
[31] K. Edalati, Z. Horita, Application of high-pressure torsion for consolidation of ceramic powders, Scripta Mater. 63 (2010) 174–177, https://doi.org/10.1016/j.scriptamat.2010.03.048.
[32] H. Razavi-Khosroshahi, M. Fuji, Development of metal oxide high-pressure phases for photocatalytic properties by severe plastic deformation, Mater. Trans. 60 (2019) 1203–1208, https://doi.org/10.2320/matertrans.MF201916.
[33] Y. Ikoma, Severe plastic deformation of semiconductor materials using high-pressure torsion, Mater. Trans. 60 (2019) 1168–1176, https://doi.org/10.2320/matertrans.MF201907.
[34] R.B. Figueiredo, P.R. Cetlin, T.G. Langdon, Using finite element modeling to examine the flow processes in quasi-constrained high-pressure torsion, Mater. Sci. Eng. 528 (2011) 8198–8204, https://doi.org/10.1016/J.MSEA.2011.07.040.
[35] R.B. Figueiredo, P.H.R. Pereira, M.T.P. Aguilar, P.R. Cetlin, T.G. Langdon, Using finite element modeling to examine the temperature distribution in quasi-constrained high-pressure torsion, Acta Mater. 60 (2012) 3190–3198, https://doi.org/10.1016/j.actamat.2012.02.027.
[36] K. Edalati, Y. Hashiguchi, P.H.R. Pereira, Z. Horita, T.G. Langdon, Effect of temperature rise on microstructural evolution during high-pressure torsion, Mater. Sci. Eng. 714 (2018) 167–171, https://doi.org/10.1016/j.msea.2017.12.095.
[37] M.I. Khan, A.O. Mostafa, M. Aljarrah, E. Essadiqi, M. Medraj, Influence of cooling rate on microsegregation behavior of magnesium alloys, J. Mater. 2014 (2014) 1–18, https://doi.org/10.1155/2014/657647.
[38] M. Klinger, A. Jäger, Crystallographic Tool Box (CrysTBox): automated tools for transmission electron microscopists and crystallographers, J. Appl. Crystallogr. 48 (2015) 2012–2018, https://doi.org/10.1107/S1600576715017252.
[39] X. Li, R.J. Dippenaar, J.K. Han, M. Kawasaki, K.D. Liss, Phase transformation and structure evolution of a Ti-45Al-7.5Nb alloy processed by high-pressure torsion, J. Alloys Compd. 787 (2019) 1149–1157, https://doi.org/10.1016/j.jallcom.2019.02.174.
[40] J.A. Del Valle, M.T. Pérez-Prado, O.A. Ruano, Deformation mechanisms responsible for the high ductility in a Mg AZ31 alloy analyzed by electron backscattered diffraction, Metall. Mater. Trans. A Phys. Metall. Mater. Sci. 36 (2005) 1427–1438, https://doi.org/10.1007/s11661-005-0235-8.
[41] Z.R. Zeng, M.Z. Bian, S.W. Xu, C.H.J. Davies, N. Birbilis, J.F. Nie, Effects of dilute additions of Zn and Ca on ductility of magnesium alloy sheet, Mater. Sci. Eng. 674 (2016) 459–471, https://doi.org/10.1016/j.msea.2016.07.049.
[42] V.I. Skrytnyy, M. V Gavrilov, T.P. Khramtsova, A.S. Kolyanova, A.S. Krasnov, S. V Porechniy, V.N. Yaltsev, Misorientation distribution function of crystals, KnE Mater. Sci. 4 (2018) 342, https://doi.org/10.18502/kms.v4i1.2185.
[43] S.-Y. Chang, S.-W. Lee, K.M. Kang, S. Kamado, Y. Kojima, Improvement of mechanical characteristics in severely plastic-deformed Mg alloys, Mater. Trans. 45 (2005) 488–492, https://doi.org/10.2320/matertrans.45.488.
[44] I. Pospíšilová, D. Vojtěch, Mechanical properties of Zn-Mg alloys, Metal 15 (2013) 15–17.
[45] M. Kawasaki, Different models of hardness evolution in ultrafine-grained materials processed by high-pressure torsion, J. Mater. Sci. 49 (2014) 18–34, https://doi.org/10.1007/s10853-013-7687-9.
[46] H. Kooiker, E.S. Perdahcioğlu, A.H. van den Boogaard, A continuum model for the effect of dynamic recrystallization on the stress-strain response, Materials 11 (2018), https://doi.org/10.3390/ma11050867.
[47] M. Kawasaki, R.B. Figueiredo, Y. Huang, T.G. Langdon, Interpretation of hardness evolution in metals processed by high-pressure torsion, J. Mater. Sci. 49 (2014) 6586–6596, https://doi.org/10.1007/s10853-014-8262-8.